Nucl. Sci. and Tech., Vol.9, No. 4 (2019), pp. 01-08

Nuclear Science and Technology

Journal homepage: https://jnst.vn/index.php/nst

Bubble behavior in liquid-gas two-phase flow behind a cross-shaped obstacle in a vertical circular duct

K. Takase*, G. Kawasaki, K. Ueta

**Department of Nuclear System Safety Engineering, Nagaoka University of Technology, Japan*
E-mail: takase@vos.nagaokaut.ac.jp

Abstract: Grid spacers installed in subchannels of fuel assemblies for nuclear reactors can promote heat transfer. However, the fluid velocity and bubble behavior are greatly affected as the cross-sectional area of the flow passage changes. Therefore, the void fraction distribution behind the obstacle that simulates the grid spacer shape simply was measured by using a wire mesh sensor (WMS) system. Moreover, a two-phase flow analysis was performed to investigate the effect of the obstacle on the bubble behavior in a vertical duct.

Keywords: *Bubbler, Two-phase flow, Obstacle, Vertical duct, WMS, Experiment, Analysis.*

I. INTRODUCTION

Clarifying two-phase characteristics in a nuclear reactor core is important in particular to enhance the thermo-fluid safety of nuclear reactors. Moreover, correct data on bubbly flow in subchannels with spacers are needed in order to verify two-phase flow models in conventional nuclear safety analysis codes and validate predicted data by current CFD codes like a direct two-phase flow analysis code (Douce, et al., 2010). Spacers installed in subchannels of fuel assemblies have the role of keeping the interval between adjacent fuel rods constant. Similarly, in case of PWR the spacer has also the role as the turbulence promoter. When the transient event occurs in a nuclear reactor, two-phase flow is generated by boiling of water due to heating of fuel rods. Therefore, it is important to confirm the bubbly flow behavior around the spacer. The purpose of this study is to make the effect of the spacer affecting the bubbly flow clear and obtain code validation data. So bubble dynamics around the simply simulated spacer was visually observed and the void fraction and interfacial velocity distributions just behind the simulated spacer was measured.

II. EXPERIMENTAL METHOD

1. Experimental Apparatus

The experimental apparatus mainly consists of a measuring section and water/air supply lines and is shown in Fig. 1. The measuring section includes a vertical flow channel with a diameter of 58 mm made of an acrylic resin, inlet and outlet plenums, and an air injection nozzle with 120 injection holes with a diameter of 0.6 mm. Water flows through the inlet plenum into the flow channel and goes up through the measuring section to the outlet plenum. Air is supplied from the air injection nozzle into the flow channel. As a result, water is mixed with air and then a water-air two-phase flow is formed as can be seen in Fig. 2. Bubbly flow conditions are determined by both flow rates of water and air.

https://doi.org/10.53747/jnst.v9i4.132
Received 07 November 2019, accepted 26 December 2019

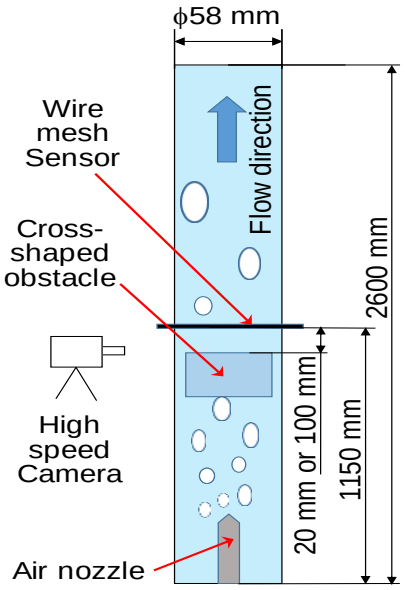

Fig. 1. Outline of an experimental apparatus

Fig. 2. Observed rising bubbles in a flow channel

2. Wire-Mesh Sensor System

The void fraction distribution at the horizontal cross- section in the flow channel is measured with a wire-mesh sensor (WMS) system (Prasser et al., 1998; 2000; 2001). Complicated behavior of an interface between water and air of each bubble is visually observed with a high speed camera (HSC). Moreover, two-phase pressure loss is measured with seven differential pressure transducers installed in the arbitrary locations in the vertical direction of the flow channel. In addition, both flow rates, pressures and temperatures of water and air are measured at the water/air supply piping lines.

The WMS can obtain the void fraction distribution in a cross-section of the flow channel by measuring the electric current from the transmitter-side wire layer through the fluid to the receiver-side wire layer. Both wire layers consist of nine wires respectively and are installed in the flow channel with the distance of 3 mm in the flow direction. The wire diameter is 0.3 mm. Appearance and measuring wires of the WMS are shown in Fig. 3. A mearing method with the WMS is as follows.

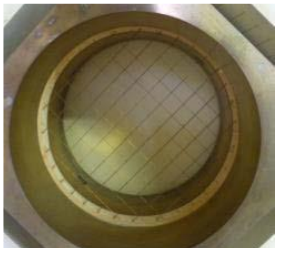

Appearance of a wire-mesh sensor

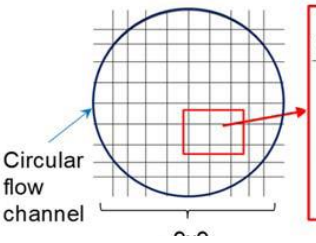

Clipped layout of each wire

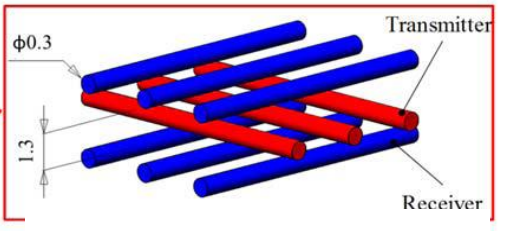

Layout of each wire of transmitter and receiver in the vertical direction (Dimension: mm)

Fig. 3. Appearance and layout of a wire-mesh sensor in a circular flow channel

1) Current is given to the transmitter-side wire layer;

2) The current flows from the transmitter-side wire layer through the fluid to the receiver-side wire layer;

3) The voltage is measured at the location where each wire intersects; and,

4) Void fraction between both wires is obtained.

The following equation is used for the conversion from the voltage to the void fraction.

$$\alpha_{i,j} = \frac{U_L - U_{i,j}}{U_L - U_G} \tag{1}$$

Here, α is the local void fraction, (i, j) is the position where two wires intersect in the cross-section of the flow channel, U[V] is the voltage measured by the WMS at two-phase flow condition, Each of U_L [V] and U_G [V] is the voltage measured by the WMS at the single-phase flow condition of liquid or gas.

On the other hand, gas-liquid interface velocity is determined using the time-series void fraction data measured by a couple of the WMS layers which are installed upstream and downstream of the flow channel. Two void fraction data by both WMS layers are compared. In Fig 4, time difference, τ, in case that the cross-correlation coefficient between both void fraction data shows the highest match is identified. Finally, the gas-liquid interface velocity, u_b, is calculated by Eq. (2) using S and τ. Here, S is the distance between both receiver-side wire layers.

$$u_b = \frac{S}{\tau} \tag{2}$$

Moreover, the cross-correlation coefficient used to obtain the interfacial velocity is obtained from the relationship between both data measured by a couple of the WMS layers and is expressed by the following equation.

$$cor(\tau) = \frac{\sum_{t=1}^{n}\left(x_t - \bar{x}\right)\left(y_{t+\tau} - \bar{y}\right)}{\sqrt{\sum_{t=1}^{n}\left(x_t - \bar{x}\right)^2\left(y_{t+\tau} - \bar{y}\right)^2}} \tag{3}$$

Here, x and y represent time series void fraction data measured with the WMS installed upstream in the flow direction and the WMS installed downward. The n shows the number of comparison data. The cross-correlation coefficient, $cor(\tau)$ has the value from -1 to 1, and it shows 1 when both data of x and y have the positive correlation, -1 when those are the negative correlation, and 0 when those have no correlation.

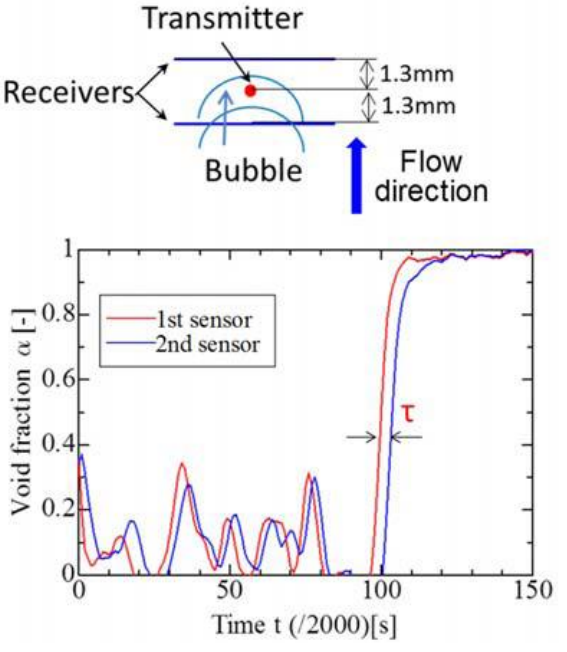

Fig. 4. Example of time variation of void fraction data at the different vertical positions

3. Experimental Conditions

The present experiments were performed under the conditions of room temperature, atmospheric pressure and non-heated isothermal flow. Working fluids are water and air. Superficial velocities of water and air, J_L and J_G, are set to be 0.13-1.0 m/s for J_L, and 0.025-0.4 m/s for J_G. Experimental conditions of J_L and J_G are shown in Table I and Table II.

Table I. Experimental Conditions of Superfacial Velocity of Water in Mixture, J_L

Case	J_{G1}	J_{G2}	J_{G3}	J_{G4}
J_G (m/s)	0.025	0.05	0.1	0.2

Table II. Experimental Conditions of Superfacial Velocity of Gas in Mixture, J_G

Case	J_{L1}	J_{L2}	J_{L3}	J_{L4}
J_L (m/s)	0.13	0.25	0.5	1.0

In order to investigate the influence of an obstacle in the flow channel to the void fraction distribution, the obstacle with the dimensions of the thickness 5 mm, the height 50 mm and the horizontal distance 58 mm as shown in Fig. 5 was installed in the position of 20 or 100 mm upstream from the WMS. The shape of the obstacle simply simulates that of the grid spacer and shows a cross-shape, but the dimensions are different.

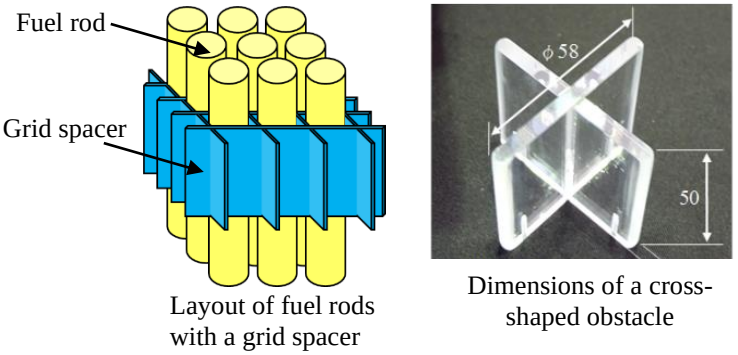

Layout of fuel rods with a grid spacer

Dimensions of a cross-shaped obstacle

Fig. 5. Appearance of a cross-shaped obstacle which simulates the shape of the grid spacer simply

III. RERULTS AND DISCUSSION.

The time-averaged void fraction distribution in the radial direction in the flow channel is indicated in Fig. 6. Here, in case of Fig. 6 (a) J_L is L_2 and in case of Fig. 6 (b) J_L is L_4. When J_G is low, the void fraction distribution shows the wall-peak distribution. On the other hand, when J_G is high, it becomes the core-peak distribution. The force which includes the lift force, etc. generates towards the wall direction in case of the small bubbles. Therefore, many small bubbles are distributed around the wall. On the other hand, the force which includes the large lift force, etc. generates to the center region of the flow channel in case of the large bubbles. As a result, many large bubbles are distributed to the center region.

Figure 7 is the bubble behavior observed with HSC. Here, the superficial velocity condition in Fig. 7 (a) are L_3 and G_1. Similarly, that in Fig. 7 (b) is L_3 and G_4. In case of Fig. 7 (a) small bubbles are observed. Meanwhile, since coalescence of

small bubbles is promoted with increasing the superficial gas velocity, the slug flow with a shape of the bullet is observed in case of Fig. 7 (b).

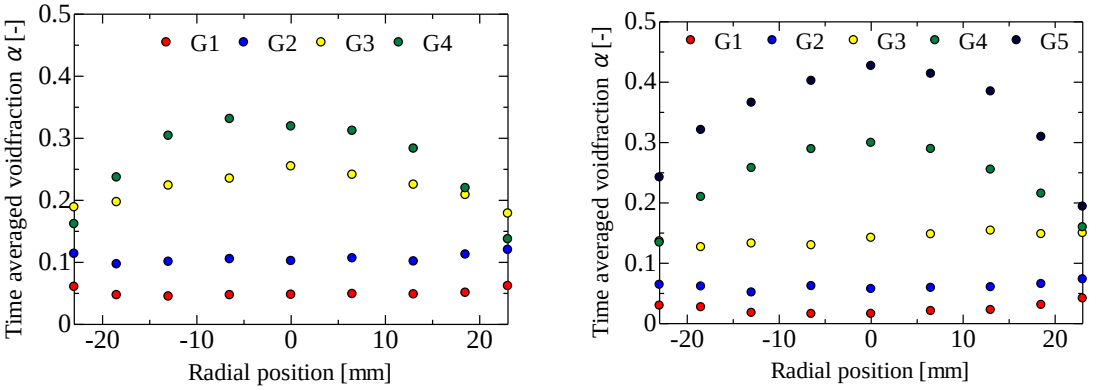

(a) In case of J_L=J_{L2} (b) In case of J_L=J_{L4}

Fig. 6. Radial void fraction distributions obtained by the conditions of J_{L2} and J_{L4}

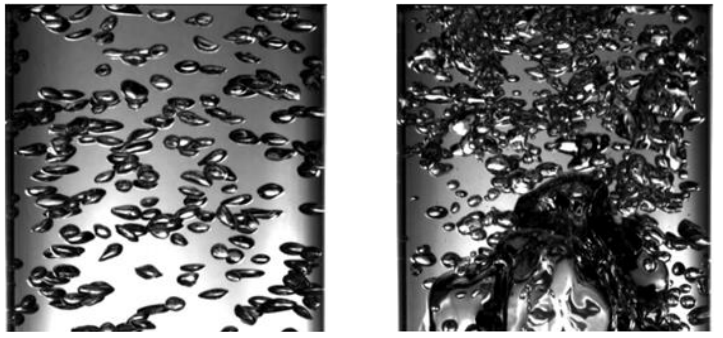

(a) In cases of J_{L3} and J_{G1} (b) In cases of J_{L3} and J_{G4}

Fig. 7. Observed bubble behavior at J_{L3}, J_{G1} and J_{G4}

Void fraction distributions in the flow channel with and without the obstacle when J_L=L_3 and J_G=G_1 are indicated in Fig. 8. Here, since measuring data in the circular flow channel are shown as a square figure, four comers in the square figure are the outside of the measuring area. The void fraction is shown with the color contour. Here, blue is 0, red is 0.2 and other colors show the value between 0 and 0.2. The void fraction distribution of Fig. 8 (a) which is the no obstacle case shows the wall peak because Gris the small bubble (i.e., bubbly flow) condition. On the other hand, Fig. 8 (b) and (c) are the results at each position of 20 or 100 mm behind the obstacle. The void fraction becomes high just behind the obstacle at Fig. 8 (b). The reason for this is that the bubbles separated at the leading edge of the obstacle coalesce just behind the obstacle. Furthermore, the void fraction becomes uniform at Fig. 8 (c). This is because the distance of 100 mm is long and the distribution is flattened.

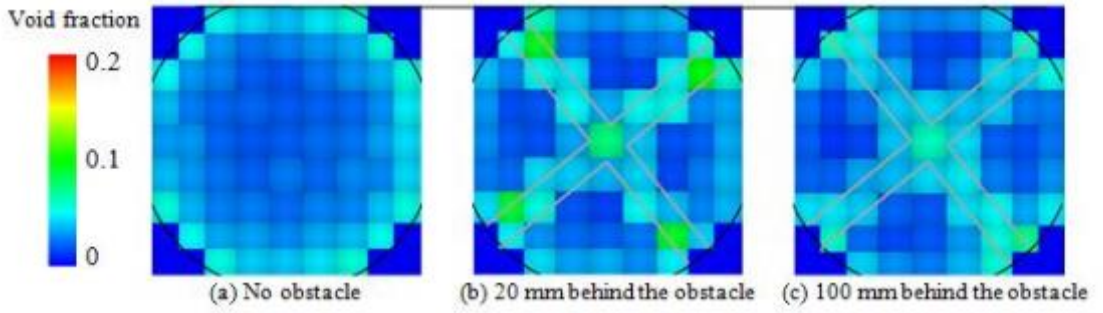

Fig. 8. Void fraction distributions at J_{L3} and J_{G1}

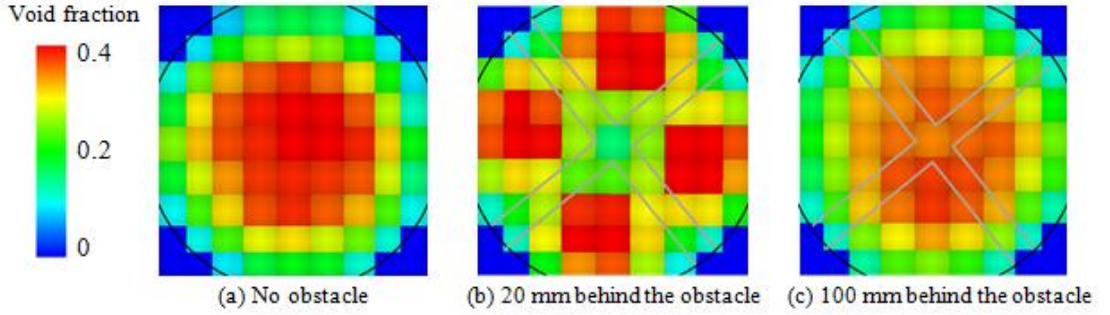

Fig. 9. Void fraction distributions at J_{L3} and J_{G5}

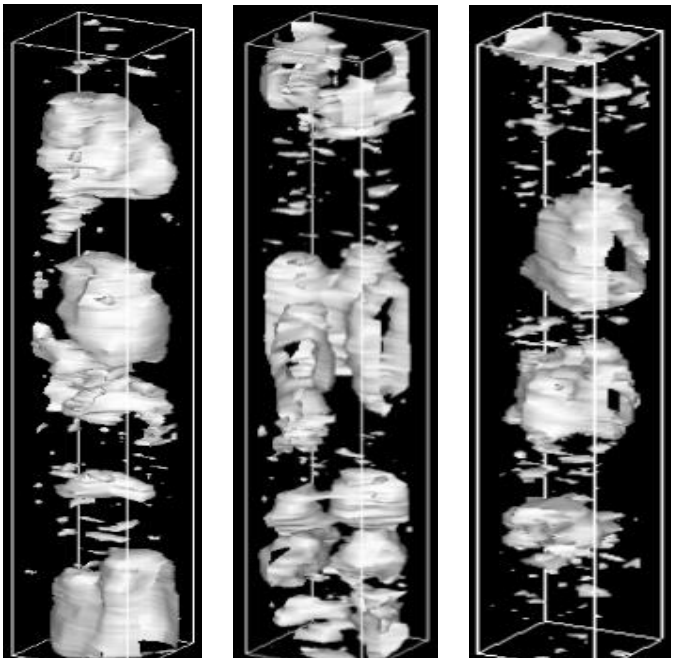

Fig.10. Three-dimensional void fraction distributions when $J_L=J_{L3}$ and $J_G=J_{G5}$

Void fraction distributions in the flow channel with and without the obstacle when $J_L=L_3$ and $J_G=G_5$ are indicated in Fig. 9. Here, blue is 0, red is 0.4 and other colors

show the value between 0 and 0.4. The void fraction distribution of Fig. 9 (a) which is the no obstacle case shows the core peak because G_5 is the large bubble (i.e., slug flow) condition. Figures 9 (b) and (c) are the results at the positions of 20 and 100 mm behind the obstacle. In Fig. 9 (b) the void fraction becomes low just behind the obstacle and high at the region except for the area just behind that. This is because large bubbles are divided by the obstacle. In Fig. 9 (c) the void fraction becomes high at the core region because the divided bubbles coalesce again.

Figure 10 shows the results of three-dimensional void fraction distribution in the case of such large bubbles. Here, Fig. 10 (a) is the result when there is no obstacle. Figure 10 (b) and (c) are the results at the positions of 20 and 100 mm behind the obstacle, respectively. Here, Fig. 10 (a) is found to be the slug flow. Also, Fig. 10 (b) shows that large bubbles are divided into four. In Fig. 10 (c), the appearance of becoming large bubbles is seen.

Figure 11 shows the void fraction distributions in the radial direction of the flow channel. Here, the vertical axis represents the local void fraction and the horizontal axis represents the dimensionless radial distance from the channel center to the side wall; r_0 and r are the radius and radial distance from the center of the circular flow channel.

The flow velocity was $J_L=L_3$ and J_G was changed to three kinds of G_1, G_3 and G_5. The open symbol shows the result in the case of no obstacle. When the flow rate is low, the void fraction distribution in the horizontal cross section of the flow channel becomes almost uniform, and shows the trend of the core peak as the flow rate increases. On the other hand, the solid symbol shows a case where there is an obstacle, and since the large bubble is divided as the flow rate increases, a high void fraction is seen near the wall of the flow channel.

Velocity distributions of the bubble interface in the flow channel with and without the obstacle when and $J_G=G_5$ arc indicated in Fiq.12. Here, blue is 0 m/s, red is 1 m/s and other colors show the velocity between 0 and 1 m/s. The velocity distribution of Fig.12 (a) which is the no obstacle case shows the core peak because G_5 is the slug flow condition. Fig.12 (b) and (c) arc the results at each position of 20 or 100 mm behind the obstacle. In Fig.12 (b) the velocity distribution of the bubble interface shows four peaks in the region where no obstacle exists. Moreover, the

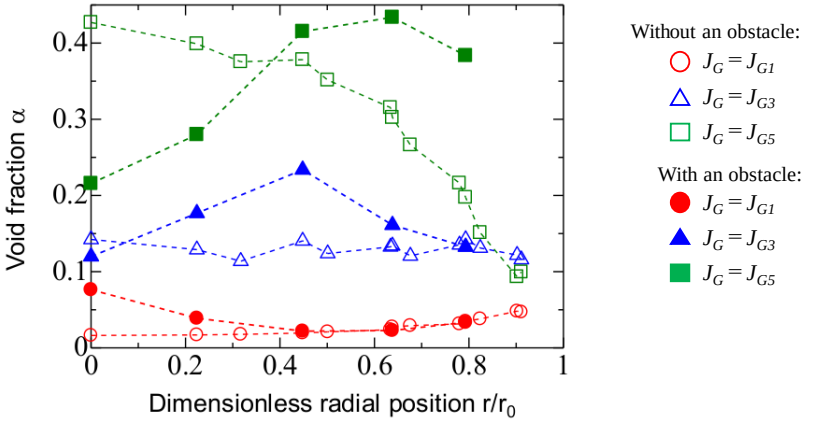

Fig. 11. Radial void fraction distributions against different J_G at the position of 20 mm behind the obstacle when $J_L=J_{L3}$

velocity distribution of the bubble interface becomes high in the core region as well as the tendency of the void fraction distribution, as can be seen in Fig. 12 (c).

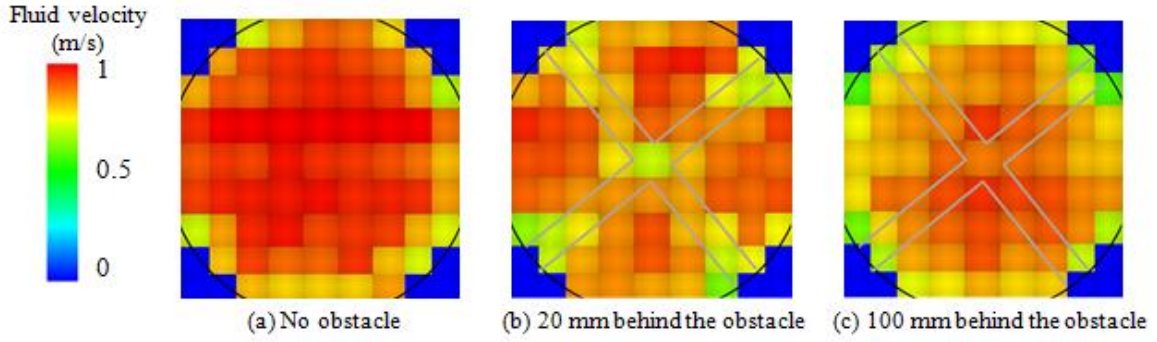

Fig. 12. Gas-liquid interface velocity distributions in the flow channel with and without the obstacle when $J_L=J_{L3}$ and $J_G=J_{G5}$

IV. CONCLUSIONS

Bubbly flow behavior, void fraction distribution and interfacial velocity distribution around the simulated spacer installed in the flow channel were investigated experimentally and at non-heated and isothermal water-air two-phase flow condition. The results of the present study arc summarized as follows:

1) When J_G is low, the void fraction distribution in the flow channel without the obstacle becomes the wall- peak distribution. When J_G is high, it becomes the core-peak distribution;

2) When J_G is low, the void fraction becomes high just behind the obstacle. The reason is that the bubbles separated at the leading edge of the obstacle coalesce just behind the obstacle;

3) When J_G is high, the void fraction becomes low just behind the obstacle and high at the region except for the area just behind that. This is because large bubbles are divided by the obstacle;

4) Behind the obstacle, the distribution of the void fraction at the channel cross section is flattened as the distance from the obstacle increases; and,

5) The gas-liquid interface velocity can be predicted from the distribution of the void fraction by using the equation of the cross-correlation coefficient.

REFERENCES

[1]. Prasser, H. M., Böttger, A. and Zschau, J., "A New Electrode-Mesh Tomograph for Gas-Liquid Flows," *Flow Measurement and Instrumentation*, 9, 1998.

[2]. H. M. Prasser, H. M., Krepper E. and Lucas, D., "Fast Wire-Mesh Sensors for Gas-Liquid Flows and Decomposition of Gas Fraction Profiles According to Bubble Size Classes", *Second Japanese-European Two-Phase Flow Group Meeting*, Tsukuba, Japan, September, 25-29, 2000.

[3]. Prasser, H. M., Scholz, D., and Zippe, C., 2001, "Bubble Size Measurement Using Wire-Mesh Sensors", *Flow Measurement and Instrumentation*, 12, 4, 2001.

[4]. Douce1, A., Mimouni1, A.., Guingo1, M., Morel2, M., J. Laviéville1, J. and Baudry1, C., "Validation of Neptune CFD 1.0.8 for Adiabatic Bubbly Flow and Boiling Flow", CFD4NRS-3, September, 14-16, Washington DC, USA, 2010.